Objective Satellite-Based Detection of Overshooting Tops Using Infrared Window Channel Brightness Temperature Gradients

KRISTOPHER BEDKA, JASON BRUNNER, RICHARD DWORAK, WAYNE FELTZ, JASON OTKIN, AND THOMAS GREENWALD

Cooperative Institute for Meteorological Satellite Studies, University of Wisconsin—Madison, Madison, Wisconsin

(Manuscript received 19 May 2009, in final form 31 August 2009)

ABSTRACT

Deep convective storms with overshooting tops (OTs) are capable of producing hazardous weather conditions such as aviation turbulence, frequent lightning, heavy rainfall, large hail, damaging wind, and tornadoes. This paper presents a new objective infrared-only satellite OT detection method called infrared window (IRW)-texture. This method uses a combination of 1) infrared window channel brightness temperature (BT) gradients, 2) an NWP tropopause temperature forecast, and 3) OT size and BT criteria defined through analysis of 450 thunderstorm events within 1-km Moderate Resolution Imaging Spectroradiometer (MODIS) and Advanced Very High Resolution Radiometer (AVHRR) imagery. Qualitative validation of the IRW-texture and the well-documented water vapor (WV) minus IRW BT difference (BTD) technique is performed using visible channel imagery, CloudSat Cloud Profiling Radar, and/or Cloud-Aerosol Lidar and Infrared Pathfinder Satellite Observation (CALIPSO) cloud-top height for selected cases. Quantitative validation of these two techniques is obtained though comparison with OT detections from synthetic satellite imagery derived from a cloud-resolving NWP simulation. The results show that the IRW-texture method false-alarm rate ranges from 4.2% to 38.8%, depending upon the magnitude of the overshooting and algorithm quality control settings. The results also show that this method offers a significant improvement over the WV-IRW BTD technique. A 5-yr *Geosynchronous Operational Environmental Satellite (GOES)-12* OT climatology shows that OTs occur frequently over the Gulf Stream and Great Plains during the nighttime hours, which underscores the importance of using a day/night infrared-only detection algorithm. *GOES-12* OT detections are compared with objective Eddy Dissipation Rate Turbulence and National Lightning Detection Network observations to show the strong relationship among OTs, aviation turbulence, and cloud-to-ground lightning activity.

1. Introduction and background

An overshooting convective cloud top is defined by the American Meteorological Society's *Glossary of Meteorology* (Glickman 2000) as "a domelike protrusion above a cumulonimbus anvil, representing the intrusion of an updraft through its equilibrium level." Overshooting tops (OTs) indicate the presence of a deep convective storm with an updraft of sufficient strength to penetrate through the tropopause and into the lower stratosphere. OTs have been identified as localized sources of lower-stratospheric water vapor (WV) through cloud-resolving NWP modeling (Wang 2003; Chemel et al. 2008) and weather satellite observation inferences (Setvak et al. 2008b), which has important implications for the earth's radiative balance and climate.

Thunderstorms with OTs frequently produce hazardous weather at the earth's surface such as heavy rainfall, damaging winds, large hail, and tornadoes (Reynolds 1980; Negri and Adler 1981; Adler et al. 1985; Brunner et al. 2007). Thunderstorms with OTs are also often associated with strong horizontal and vertical wind shear and lightning through charge separation and accumulation in the storm updraft region (Ziegler and MacGorman 1994; Wiens et al. 2005), both of which represent serious turbulence and safety hazards for in-flight and ground aviation operations. OTs also generate gravity waves as they interact with and penetrate through the tropopause, which can produce significant turbulence at large distances from the OT (Heymsfield et al. 1991; Lane et al. 2003; Bedka et al. 2007).

Corresponding author address: Kristopher M. Bedka, Cooperative Institute for Meteorological Satellite Studies, University of Wisconsin—Madison, 1225 West Dayton St., Madison, WI 53706. E-mail: kristopher.bedka@ssec.wisc.edu

DOI: 10.1175/2009JAMC2286.1

Convectively induced turbulence (CIT) represents a significant hazard for the aviation industry. From 1992 to 2001, the Federal Aviation Administration (FAA 2004) shows that 4326 weather accidents occurred in the United States, of which 509 were cited as being related to turbulence. Nearly 23% of these CIT-related accidents resulted in fatal injuries to the occupants of the aircraft (FAA 2004). FAA (2004) also indicates that the majority (67%) of turbulence encounters over the United States for general aviation occur during the warm season (April–September). Cornman and Carmichael (1993) state that CIT is responsible for over 60% of turbulence-related aircraft accidents. Because of the hazards associated with OTs, objective detection of OTs is a product requirement for the Geostationary Observing Environmental Satellite (GOES)-R Advanced Baseline Imager (ABI) instrument program (Schmit et al. 2005). The GOES-R is currently scheduled for launch in 2015.

Signatures in multispectral weather satellite imagery indicate the presence of OTs. OTs exhibit a lumpy or ''cauliflower'' textured appearance in visible channel imagery. OTs are also inferred through the presence of a small cluster of very cold brightness temperatures (BTs) in the ~11-μm infrared window (IRW) region. OTs continue to cool at a rate of 7–9 K km^{-1} as they ascend into the lower stratosphere (Negri 1982; Adler et al. 1983), making them significantly colder than the surrounding anvil cloud temperature. The surrounding anvil cloud has been shown to have temperatures at or near that of the tropopause level (Adler et al. 1985).

Techniques and instrumentation such as numerical modeling, aircraft photography, multisatellite stereoscopy, active space-based radar, and aircraft-based lidar have been used to better understand the relationship between OT signatures in visible and IRW satellite imagery and the physical height of the cloud top. From several flights over OTs with an airborne lidar, Heymsfield et al. (1991) showed that some OTs reach altitudes up to 2 km above the surrounding anvil cloud. From Tropical Rainfall Measuring Mission (TRMM) precipitation radar data (Kummerow and Barnes 1998), Liu and Zipser (2005) found an overshooting magnitude of 0.67 km for global deep convective clouds. The height difference between lidar and TRMM-based results is likely due to the fact that lidar derives cloud-top height via ice crystal reflectance whereas TRMM requires reflectance from precipitation particles that reside at lower levels within the cloud. Liu and Zipser also show that overshooting magnitude depends significantly on whether the level of neutral buoyancy or tropopause height is used as a reference. Currently, Moderate Resolution Imaging Spectroradiometer (MODIS) multispectral imagery, CloudSat Cloud Profiling Radar profiles, and Cloud-Aerosol Lidar and Infrared Pathfinder Satellite Observation (CALIPSO) cloud-top height retrievals from the National Aeronautics and Space Administration (NASA) A-Train satellite constellation can be used to better understand the relationship between satellite OT inferences and the physical cloud height (Stephens et al. 2002; Mitrescu et al. 2008).

Several published studies describe objective OT detection techniques using multispectral satellite imagery. Berendes et al. (2008) show that a combination of visible and near-IR texture and reflectance, IR channel BTs, and multispectral IR channel BT differences (BTD) can be used in an unsupervised cloud classification technique to objectively detect deep convection and OTs. While this technique performs well at and around the hours near solar noon, Berendes et al. show a significant diurnal signal in classifier output that can be induced by enhanced texture in visible channel imagery atop deep convective clouds at low solar zenith angles. A close inspection of OT detections during the early morning and evening hours with corresponding visible and IRW channel imagery suggests that many of these pixels would be considered false alarms. Near-IR reflectance and ice particle effective radius techniques (Lindsey and Grasso 2008; Rosenfeld et al. 2008) suffer from some of the same issues, making these techniques unreliable for and/or not applicable to objective day/night OT detection.

As the GOES-R ABI satellite program and operational forecasters require product availability during both day and night, the use of infrared-only techniques for objective OT detection has also been investigated. The 6–7-μm water vapor absorption minus the ~11-μm IRW channel BT difference technique for OT detection has been described extensively in the literature (Fritz and Laszlo 1993; Ackerman 1996; Schmetz et al. 1997; Setvak et al. 2007; Martin et al. 2008). The premise behind the use of this technique for OT detection is that 1) the atmospheric temperature profile warms with height in the lower stratosphere, 2) water vapor is forced into the lower stratosphere at levels above the physical cloud top by the overshooting storm updraft, 3) this water vapor emits at the warmer stratospheric temperature whereas emission in the IR window channel originates from the colder physical cloud top, and 4) positive differences between the warmer WV and colder IRW BTs can therefore identify where overshooting is occurring. The maximum WV-IRW BTD can be offset from the OT location because of advection of stratospheric water vapor away from the active thunderstorm updraft (Setvak et al. 2007) or from other remote sources not related to overshooting convection.

The WV-IRW BTD literature cited in the preceding paragraph indicates that the required WV-IRW BTD threshold for OT detection can vary depending upon satellite instrument spatial resolution and spectral channel coverage, intensity of the convective updraft, stratospheric lapse rate, and water vapor residence time in the stratosphere. For 4-km *GOES-12* imagery, a BTD value greater than +1 K is shown to relate to the presence of overshooting (Martin et al. 2008). For 1-km MODIS imagery, this BTD value would detect a substantial portion of the anvil in addition to OT pixels, resulting in a large number of false alarms. A BTD value of +2 K is shown to be a better indicator of overshooting in this higher-resolution imagery.

One characteristic of OTs that has yet to be utilized in a published objective detection method is the fact that these features appear as small clusters of very cold pixels relative to the surrounding thunderstorm anvil. Spatial IRW BT gradients (IRW-texture hereinafter) can be combined with NWP-based tropopause temperature information and knowledge of the characteristic size of an OT to objectively identify them at their proper scale. Such a technique would have some advantages over the WV-IRW BTD in that 1) it is not explicitly affected by the spatial/vertical distribution of atmospheric water vapor, 2) it does not overdiagnose the size of an individual OT, and 3) it does not use WV BT information, which can be affected by variation in the central wavelength and/or spectral coverage of the WV absorption channel.

This paper introduces an IRW-texture–based objective OT detection technique developed at the University of Wisconsin—Madison Cooperative Institute for Meteorological Satellite Studies (UW-CIMSS) for the GOES-R ABI instrument program. This technique is applied to *GOES-12*, MODIS from the NASA Earth Observation System (EOS) *Aqua* satellite, and synthetic GOES-R ABI imagery to demonstrate detection capability for a variety of current and future sensors. The accuracy of this method is determined through comparison to OTs identified in visible channel imagery, NASA CloudSat and CALIPSO observations, and cloud-resolving NWP model cloud-top height. Qualitative and quantitative comparisons between the IRW-texture and the WV-IRW BTD technique are also shown to illustrate performance of the IRW-texture technique relative to an existing, well-documented method. A 5-yr climatology of OTs across the eastern United States is produced to show where and when OTs are most frequently detected in *GOES-12* imagery. *GOES-12* IRW-texture–based OT detections are also compared to objective turbulence and cloud-to-ground lightning strikes to show the relationship between OTs and these aviation hazards.

2. Datasets

a. Overshooting-top detection algorithm inputs

1) SATELLITE IMAGERY

GOES-12 and *Aqua* MODIS IRW BTs are used as the primary satellite inputs to the IRW-texture detection method in this paper. MODIS is kept at its native 1-km resolution to show OT detection capability from the highest-quality data, and it is also degraded to a 2-km resolution through the use of a Gaussian point spread function to simulate future GOES-R ABI imagery (Lindstrom et al. 2008). *GOES-12* data are provided by the UW Space Science and Engineering Center (SSEC) data center. MODIS data are acquired from the NASA Level 1 Atmosphere Archive and Distribution System (LAADS). Though GOES- and MODIS-based OT detections are featured in this paper, this technique can be applied to any imager with high spatial resolution (<5 km) and an ~11-μm IRW channel.

The IRW-texture detection technique is compared to the WV-IRW BTD as well as visible channel imagery. For the comparisons in this paper, the 6.5- (*GOES-12*) and 6.7-μm (MODIS) WV BTs are kept at their native resolution to show WV-IRW BTD output that would be operationally available to users. An Interactive Data Language routine from L. Gumley (UW-SSEC) was utilized for removing line-to-line inconsistencies (i.e., "stripes") that are evident in MODIS Level 1B BTs. Visible imagery from 0.25 (MODIS) to 1 km (MODIS and GOES) is used for qualitative validation, where the characteristic lumpy texture and shadowing associated with OTs are compared with infrared-based detections during daylight hours.

2) NWP TROPOPAUSE TEMPERATURE

A 6-h forecast of tropopause temperature from the 0.5° resolution Global Forecast System (GFS) NWP model is also used as input to the IRW-texture OT detection algorithm, though this method can use any NWP model with tropopause temperature output. The GFS model is provided via the NOAAPORT data feed to the UW-SSEC data center. The 6-h forecast is used to emulate the algorithm processing and performance that would occur in real time. This NWP field is remapped to the resolution and projection of the corresponding satellite imagery using the Man Computer Interactive Data Access System (McIDAS-X) software package (Lazzara et al. 1999) so that a tropopause temperature is associated with every satellite pixel.

b. Validation and comparison datasets

1) CLOUDSAT AND CALIPSO

The CloudSat and CALIPSO satellites fly as part of a constellation of satellites referred to as the A-Train

that also includes Polarization and Anisotropy of Reflectances for Atmospheric Sciences Coupled with Observations from Lidar (PARASOL) and the NASA EOS *Aqua* and *Aura* (Stephens et al. 2002). The 1-km-spatial-resolution, Level 2, cloud-top-height product from CALIPSO and 1.4-km field-of-view resolution CloudSat Cloud Profiling Radar reflectivity factor (i.e., 2B-GEOPROF) products were analyzed to identify cases with direct OT overpasses, which serve as an independent verification of MODIS-based OT detections. These products were acquired from the NASA Langley and Colorado State University archives, respectively. Collocated Goddard Earth Observing System Model, Version 5, (GEOS-5) tropopause height analyses present within the CALIPSO cloud-top height HDF format file are plotted with the CALIPSO and CloudSat observations to verify the presence and magnitude of the overshooting. *Aqua* MODIS collects observations approximately 2 min ahead of CloudSat and CALIPSO. As OTs are often rapidly evolving phenomena, this can lead to some mismatch between the OT characteristics observed by MODIS and these two satellites, though a mismatch is not apparent in the example shown in section 4b.

2) Simulated GOES-R ABI proxy imagery and WRF NWP lower-stratospheric microphysical content

Version 2.2 of the Advanced Research Weather Research and Forecasting model (ARW-WRF; Skamarock et al. 2007) was used to generate a high-resolution simulation of a widespread convective storm event that occurred over the central United States. The simulation was initialized at 0000 UTC 4 June 2005 using 1° GFS data and then integrated for 30 h on a single 3460 × 2050 grid point domain covering the continental United States (CONUS) with 2-km horizontal grid spacing and 52 vertical levels. Simulated temperature, moisture, and cloud data were subsequently passed through the Successive Order of Interaction Forward Radiative Transfer Model (Heidinger et al. 2006) to generate simulated ABI infrared BTs with 5-min temporal resolution over a 2-h period from 2200 UTC 4 June to 0000 UTC 5 June. A full description of the process used to generate these synthetic BTs and validation relative to Meteosat Second Generation (MSG) Spinning Enhanced Visible and Infrared Imager (SEVIRI; Schmetz et al. 2002) observations is provided by Otkin et al. (2009). The IRW-texture and WV-IRW BTD OT detection techniques are applied to the synthetic GOES-R ABI imagery to identify potential overshooting pixels. For this study, the synthetic ABI 11.2-μm channel is used as the IRW channel and the ABI 6.2-μm channel is used for WV. The 6.2-μm channel has similar central wavelength to that of the MSG SEVIRI and is used in the WV-IRW BTD by Setvak et al. (2007) for OT detection.

ARW model output is used here to identify "truth" OT pixels and validate synthetic ABI-based detections. This comparison is trivial as ARW output is used to generate the synthetic GOES-R ABI BTs and the map projection and horizontal resolution of the two datasets are an exact match. The total hydrometeor mixing ratio (THMR), which represents a summation of the rain, graupel, snow, pristine crystal, and cloud liquid water content at each ARW model vertical level, is used to define the truth OT locations. Animated ARW cloud isosurfaces and vertical motion fields show that anomalously large THMR values in the lower stratosphere are indicative of strong thunderstorm updrafts and OTs. An example of the relationship between two OTs and the ARW THMR at 200, 175, and 150 hPa is shown in Fig. 1. OTs are found to correlate well with anomalously large THMR values at and above 175 hPa. The THMR thresholds used to define truth OT pixels and the methodology for this quantitative validation are described in section 3.

3) Eddy dissipation rate turbulence observations

Eddy dissipation rate (EDR) observations from commercial aircraft provide an objective measure of the vertical accelerations induced by turbulent atmospheric phenomena upon an aircraft (Cornman et al. 1995). This dataset is produced through the combination of existing aircraft sensors, avionics, and communication networks, producing "state of the atmosphere" turbulence diagnostic (Sharman et al. 2006). United Airlines Boeing 737 and 757 aircraft began collecting these EDR data in 1997. The EDR observing system was designed to provide routine and quantitative measurements of atmospheric turbulence intensity including null observations, addressing many of the deficiencies with pilot reports (PIREPs) (Sharman et al. 2006). EDR observations are collected every minute during flight at altitudes above 20 000 ft and are transmitted automatically to the ground. The National Center for Atmospheric Research (NCAR) Research Applications Laboratory (RAL) has provided UW-CIMSS with EDR data from January 2005 to September 2008. Over this 2005–08 time period, as many as 161 United Airlines aircraft were collecting EDR observations (G. Blackburn, NCAR RAL, 2009, personal communication). These data are used in this study to investigate the relationship between satellite observations of deep convective storms with/without OTs and observed aviation turbulence during the 2005–08

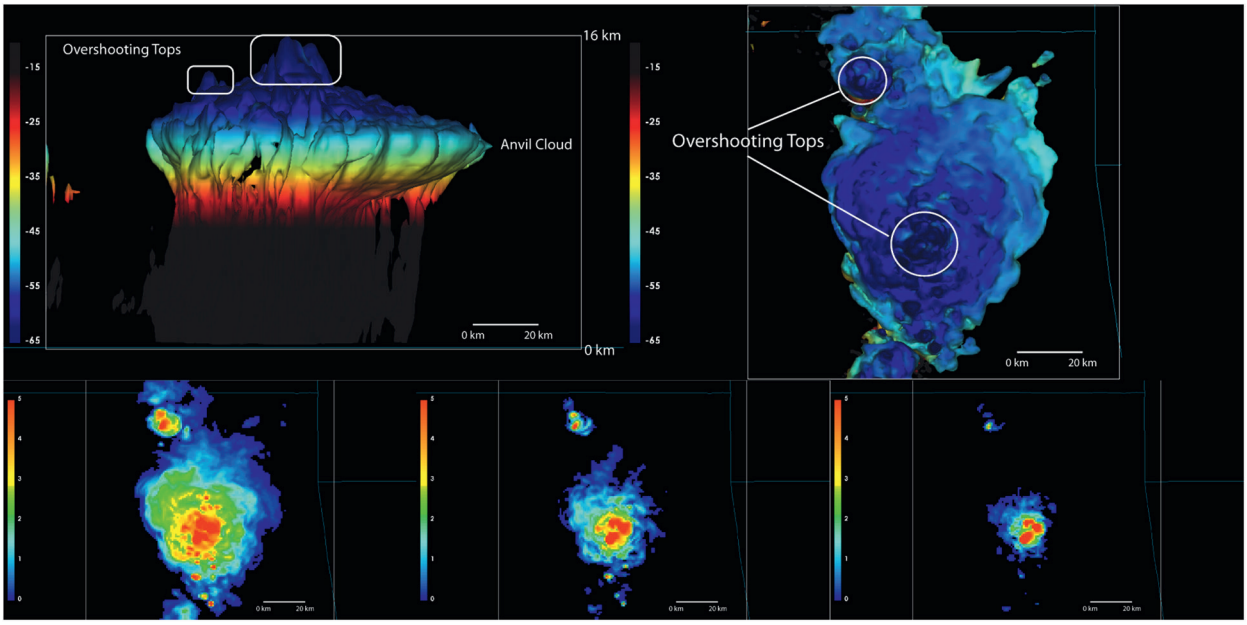

FIG. 1. (top left) A top view of the 0.05 g kg^{-1} THMR isosurface colored by simulated GOES-R ABI 11.2-μm IRW BTs. OTs appear as localized cold regions surrounded by a warmer anvil cloud. Warm temperatures for clear sky and low cloud pixels are transparent. (top right) A side view of the same isosurface showing that the two OTs have heights significantly higher than the anvil cloud. The isosurface is colored here by the ARW 3D temperature field. ARW THMR output at (bottom left) 200, (bottom middle) 175, and (bottom right) 150 hPa showing that high THMR values are associated with the OTs identified in the top panels. Graphics were produced using the McIDAS-V visualization software developed at UW-SSEC.

convective seasons (considered to be April–September in this study).

4) NATIONAL LIGHTNING DETECTION NETWORK OBSERVATIONS

The National Lightning Detection Network (NLDN; Orville 2008) detects cloud-to-ground lightning strikes in real time with over 100 sensors across the CONUS. The NLDN provides lightning flash detection efficiency near 95% and a flash location accuracy of 500 m or better during both day and night. This efficiency, positional accuracy, and geographic coverage provides a robust dataset of collocated cloud-to-ground lightning strikes and infrared satellite observations. UW-CIMSS has archived NLDN observations from May to September 2008 across CONUS that are used in this study to investigate the relationship between satellite-observed deep convective storms and cloud-to-ground lightning activity. The authors are aware that cloud-to-ground lightning strikes represent a fraction of the total lightning activity within a thunderstorm, but NLDN represents the only widely available dataset with nearly full CONUS coverage that can provide a sufficient sample size for this study. The goal of this effort is to gain an understanding of the relationship between OTs detected in readily accessible, operational geostationary satellite data and lightning strikes at the surface to determine the hazards posed by storms with OTs to the public and aviation safety.

3. Methodology

a. IRW-texture overshooting-top detection technique description

This technique combines NWP tropopause temperature output with detailed analyses of 450 archived ''enhanced (or cold) V'' producing storms identified by Brunner et al. (2007) to defines the criteria used to identify clusters of cold pixels with a size matching that of commonly observed OTs. The first step in this technique is to identify ''cold'' pixels with IRW BTs less than or equal to 215 K and the NWP tropopause temperature at that location. NWP tropopause temperature information is included to ensure that a given pixel is indeed ''overshooting'' the tropopause. Figure 2 shows that for the 450 enhanced-V–producing storms, a 215-K BT threshold would be sufficient to capture 96% of these events. Hoinka (1999) found that, from 1979 to 2003, the mean tropopause temperature over the United States ranged from 202 K in Florida to 218 K in Maine. Martin et al. (2008) also use 215 K as their ''benchmark index'' to identify deep convective cloud pixels.

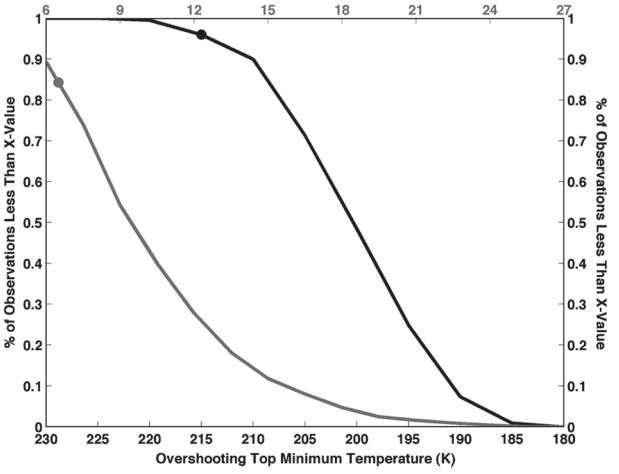

FIG. 2. The frequency of OT minimum IRW BTs less than BT values along the bottom *x*-axis scale for 450 ''enhanced V'' thunderstorms described by Brunner et al. (2007) (black line). The frequency of the OT minimum BT and mean surrounding anvil BT difference minus than BT difference values along the top *x*-axis scale for the same 450-thunderstorm database (gray line). Circles along the two lines represent criteria used in the IRW-texture OT detection method.

The next step involves sorting the list of cold pixels by their IRW BT, with the coldest pixel being first in the list. The algorithm then loops through the sorted list and computes the mean anvil temperature surrounding each pixel in the list. Through a detailed analysis of 1-km MODIS and Advanced Very High Resolution Radiometer (AVHRR) visible and IRW channel imagery for 450 thunderstorms in the Brunner et al. (2007) dataset, it was found that the largest diameter of an OT was 12 km, which is a bit larger than the 1–10-km diameter described by Fujita (1992) but smaller than some extreme overshooting events described by Liu and Zipser (2005). The use of this 12-km criterion impacts the algorithm in two ways. First, a pixel is not processed if it is within 15 km of another colder pixel in this list. This is done to ensure that the technique is not defining a new OT when a given pixel is actually part of a previously identified OT with a colder BT. Second, to ensure that only non-overshooting anvil pixel BTs are included in the mean anvil temperature, pixels at a 3 (for 4-km *GOES-12*), 4 (for 2-km simulated or ARW-based synthetic ABI), or 8 (for 1-km MODIS) pixel radius are sampled in 16 directions at equally spaced 22.5° angle intervals. The surrounding anvil pixels must have an IRW temperature of 225 K or colder to be included in the mean computation and must be present at 5 of the 16 radii. The 5 of 16 pixel criterion is imposed to ensure that the anvil is of relatively large horizontal extent, but allows an anvil to be either sufficiently large but irregularly shaped or to occupy as small as a 90° quadrant, which might be the case when strong jet-level winds are present. Cold pixels for which a mean surrounding anvil BT can be computed are considered ''candidate overshooting pixels.''

A candidate overshooting pixel is considered to be an OT if the pixel is at least 6.5 K colder than the mean surrounding anvil BT. Figure 2 shows that a 6.5-K threshold would also capture 84% of the aforementioned 450 severe storms. Negri (1982) and Adler et al. (1983) have shown that a 7–9 K km^{-1} lapse rate is present in association with OTs. Thus, a 6.5-K difference would imply that the OT is from ~0.7 to ~0.9 km above the surrounding anvil cloud.

TABLE 1. Results from a statistical comparison between OTs detected in synthetic GOES-R ABI IRW channel imagery and truth OT locations as defined by ARW THMR.

Overshooting-top detection method	False-alarm rate <175-hPa cloud-top 5 of 16 pixels included in mean (%)	False-alarm rate <165-hPa cloud-top 5 (16) of 16 pixels included in mean (%)	Percentage of total high-confidence pixels identified	No. of detected pixels 5 (16) of 16 pixels included in mean
IRW-texture OT ≥ 4.5 K colder than surrounding anvil	14.4	43.7 (32.5)	36.0	4105 (2921)
IRW-texture OT ≥ 5.5 K colder than surrounding anvil	14.0	40.9 (27.0)	35.1	3327 (2078)
IRW-texture OT ≥ 6.5 K colder than surrounding anvil	15.9	38.8 (22.7)	34.8	2440 (1603)
IRW-texture OT ≥ 7.5 K colder than surrounding anvil	13.4	35.2 (17.5)	34.8	1936 (1258)
IRW-texture OT ≥ 8.5 K colder than surrounding anvil	10.2	31.2 (14.7)	32.4	1447 (908)
IRW-texture OT ≥ 9.5 K colder than surrounding anvil	7.9	24.8 (8.6)	32.4	1145 (716)
IRW-texture OT ≥ 10.5 K colder than surrounding anvil	4.2	19.6 (4.2)	31.5	884 (566)
WV-IRW BTD ≥ 2 K	5.1	46.1	28.0	1123
WV-IRW BTD ≥ 3 K	2.3	32.6	1.5	43

A greater number of OTs could potentially be detected with a lower difference value, but this would also induce a greater number of false detections in complicated anvil scenes with spatially variable BT gradients (see Table 1). A difference value of 3.5 K would have been required to detect 100% of OTs, assuming the 16-km anvil sampling diameter described above for 2-km ABI imagery.

At this point, the coldest pixel of a given OT has been identified, which will be referred to as an OT ''center.'' To identify remaining pixels that compose a given OT, a search box is placed around a given OT center pixel to find pixels that are within a 6-km radius and at least 50% colder than the mean surrounding anvil BT. This 6-km criterion is selected because the largest OT in the analysis described above has a diameter of 12 km. As an example, if the IRW BT of the OT center is 190 K and the surrounding anvil mean BT is 210 K, then all pixels within the search box with a BT at or colder than 200 K are also considered OT pixels. The algorithm terminates after all remaining OT pixels are classified.

This technique will perform best when an anvil cloud extends at least 8 km away from a given OT pixel at 5 of the 16 radii and the coldest IRW BTs are vertically aligned with the highest cloud tops. Thus, OTs in a small, newly developing convective cloud with a limited anvil cloud extent cannot be detected through this technique. Also, an OT may not be detected when the coldest IRW BTs are offset from the highest clouds, as in situations with 1) very strong vertical wind shear and/or 2) significant mixing between the OT and ambient stratospheric air in conjunction with a strong temperature inversion. Examples of such situations are the ''class 3'' storms described by Adler and Mack (1986) and cold ring–shaped storms described by Setvak et al. (2008a). The frequency of occurrence of these class 3 storms is uncertain, but is assumed to be small relative to the total number of OT events.

b. *Validation and statistical comparisons*

The relative accuracy of the IRW-texture and WV-IRW BTD OT detection methodologies will be examined through 1) qualitative comparisons with CloudSat reflectivity factor profiles and CALIPSO cloud-top height profiles and visible channel imagery and 2) quantitative comparisons of tops detected in synthetic ABI satellite imagery with truth overshooting defined by WRF THMR. The relationships between *GOES-12* OT detections and hazards such as aviation turbulence and cloud-to-ground lightning are also determined. The methodology for these comparisons is described below.

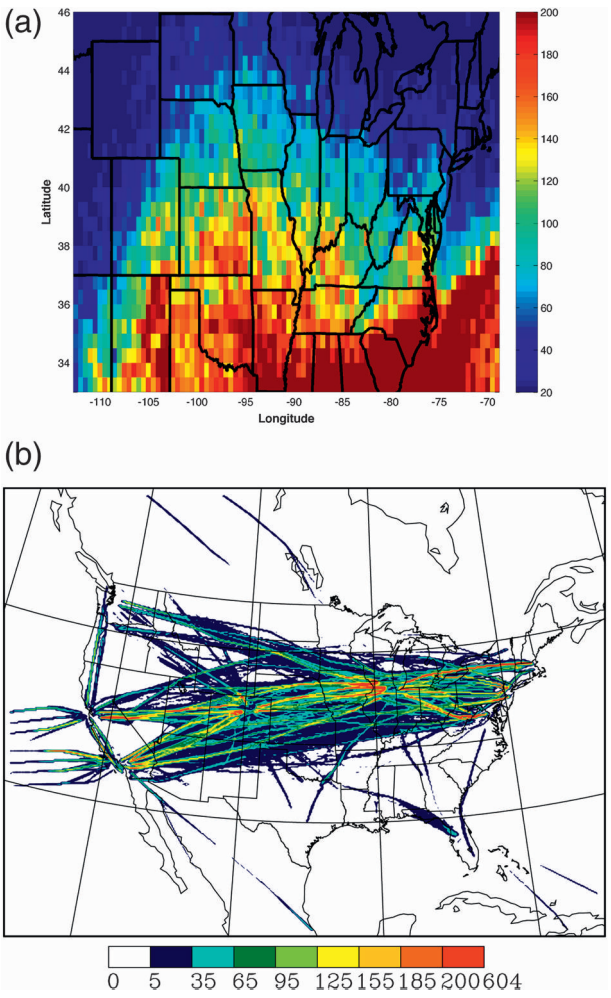

FIG. 3. (a) A climatology of OTs detected by the IRW-texture technique using *GOES-12* imagery from April to September 2004–08. (b) The flight routes of EDR-equipped United Airlines Boeing 737 and 757 aircraft. Warmer colors indicate a greater volume of air traffic.

1) MODIS WITH CLOUDSAT AND CALIPSO

Aqua MODIS imagery is used to compute both the IRW-texture and WV-IRW BTD OT detection techniques along the paths observed by CloudSat and CALIPSO. The MODIS 1-km navigation files are combined with MODIS imagery, CloudSat radar reflectivity factor, CALIPSO cloud-top height observations, and collocation files to extract MODIS 1-km BTs and WV-IRW BTD along the CloudSat/CALIPSO path. IRW-texture–based OT detections are processed separately using the degraded 2-km resolution imagery and are also collocated with the CloudSat/CALIPSO path. Cloud tops above the GEOS-5 tropopause height are considered truth OT locations that are used evaluate the characteristics of the IRW-texture and WV-IRW BTD OT detection techniques.

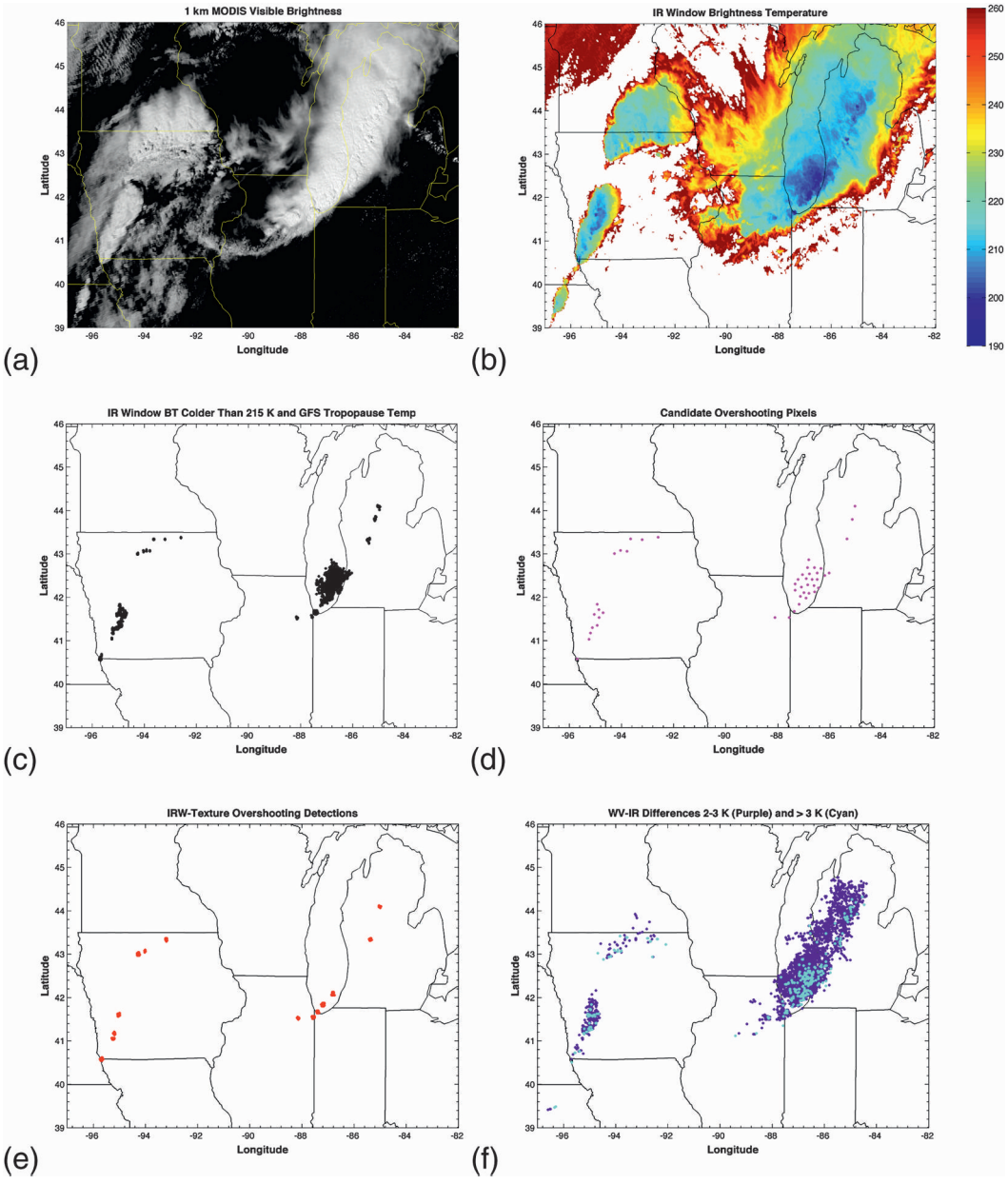

FIG. 4. (a) Contrast-enhanced *Aqua* MODIS 0.65-μm visible channel imagery at 1835 UTC 8 Jun 2008. (b) Color-enhanced *Aqua* MODIS IRW imagery at the same date and time. (c) Pixels with IRW BTs colder than 215 K and the GFS tropopause temperature. (d) Candidate overshooting pixels within the IRW-texture method. (e) IRW-texture OT detections. (f) WV-IRW BT differences between 2 and 3 K (purple) and >3 K (cyan).

2) PROXY ABI WITH WRF NWP THMR

Five-minute resolution synthetic ABI imagery between 2200 UTC 4 June and 0000 UTC 5 June 2005 over CONUS is used as input to the IRW-texture and WV-IRW BTD techniques. The cloud-top height is defined as the highest model level where a THMR ≥ 0.05 g kg^{-1} is present. During this time period, the tropopause is found to be at ~175 hPa (~13 km) over the convectively active portion of the domain. As the ARW simulation at these levels has a 0.5-km vertical resolution, ABI OT detections are compared with two sets of pixels, those with cloud tops above 175 and 165 hPa (~13.5 km). As the two algorithms being evaluated in this study may detect overshooting of varying magnitude, these two truth OT criteria are set to include both marginal (175–165 hPa, 0–0.5-km overshooting magnitude) and more significant (<165 hPa, >0.5 km) OT occurrences.

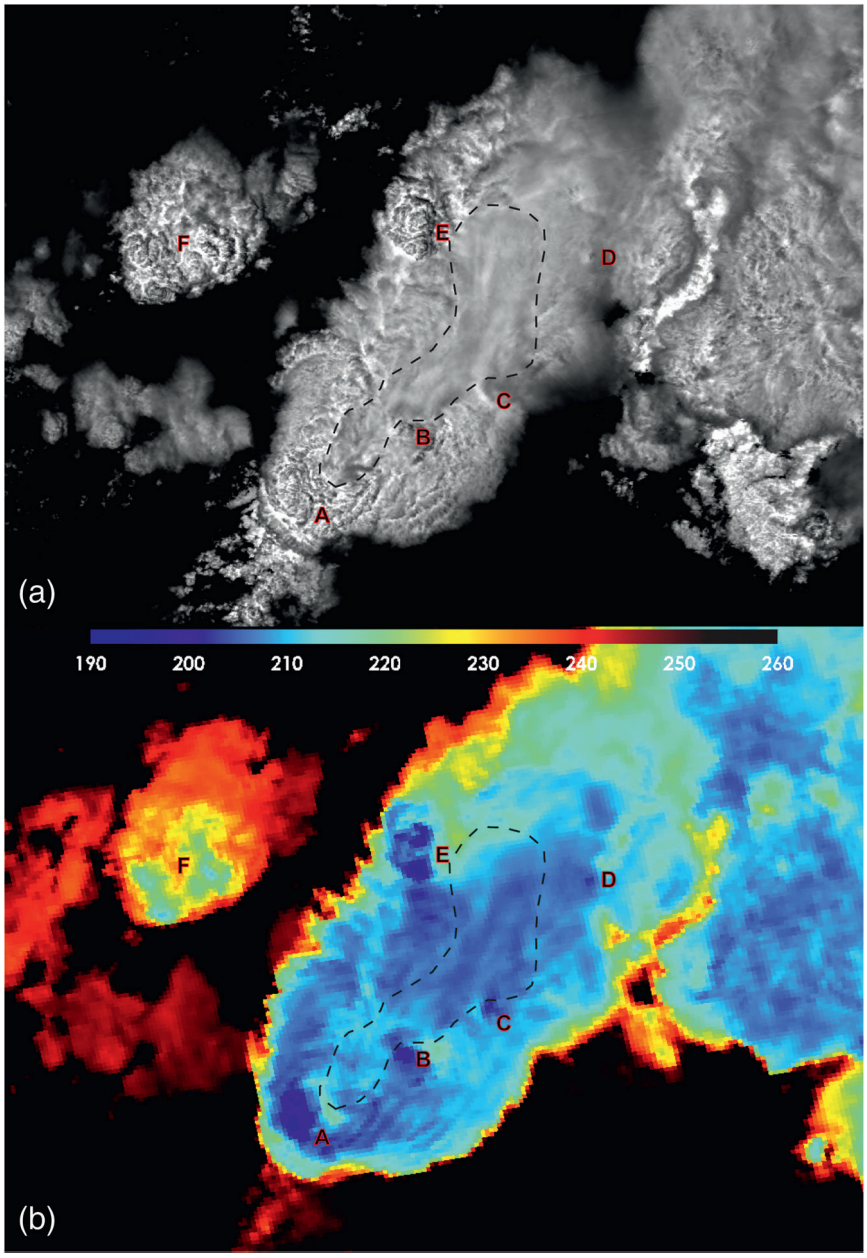

FIG. 5. (a) Contrast-enhanced *Aqua* MODIS 0.25-km visible channel image at 2005 UTC 13 Jun 2003 over the Texas Panhandle. (b) Color-enhanced *Aqua* MODIS 1-km IRW BT channel image at the same date and time. The BT color scale is provided along the top of (b). Selected portions of the storms are labeled with the letters A–F to improve the clarity of the figure and supporting discussion. An above-anvil cirrus plume is outlined by a dashed line.

A second and possibly better indicator of algorithm performance involves comparison of synthetic ABI-based OT detections to a smaller set of ''high confidence'' OT pixels. These pixels are defined using two criteria: 1) cloud-top heights $\leq$ 125 hPa ($\sim$15 km) and 2) an anomalously high THMR at the tropopause. Based upon these criteria, the pixels would be associated with intense vertical motions in the upper troposphere and lower stratosphere and would correlate well with significant overshooting. To determine anomalously high tropopause THMR, 175-hPa ARW THMR values are accumulated across the entire CONUS domain over the 2-h study ARW period and those with a THMR exceeding the 99th percentile are considered high-confidence OT pixels.

OT pixels identified by the IRW-texture and WV-IRW BTD techniques are compared with these two sets

of truth pixels to derive quantitative performance statistics. Two statistics will be used to evaluate the relative accuracy of the IRW-texture and the WV-IRW BTD techniques: 1) false-alarm rate (FAR) and 2) probability of high-confidence OT pixel detection (POD). The false-alarm rate is defined as

$$\text{FAR} = \frac{\text{Number of Incorrect OT Pixel Detections}}{\text{Total Number of OT Pixel Detections}}.$$

The probability of high-confidence OT pixel detection is defined as

$$\text{POD} = \frac{\text{Total Number of Correctly Identified High-Confidence OT Pixels}}{\text{Total Number of High-Confidence OT Pixels}}.$$

3) EDDY DISSIPATION RATE TURBULENCE

The IRW-texture OT detection algorithm is applied to *GOES-12* imagery from April to September 2005–08 and compared with EDR turbulence observations over the domain shown in Fig. 3a. An example of the density of United Airlines aircraft flights observing EDR across CONUS is shown in Fig. 3b. All 85 operational *GOES-12* scans that observe CONUS per day are processed within the IRW-texture algorithm. Satellite pixels are parallax corrected based on a cloud-top height of 14 km to better match locations of EDR observations. EDR observations are compared with OTs if they are within of ±5 min of a given satellite image. Both OT pixels and candidate OT pixels that are not at least 6.5 K colder than the surrounding anvil (i.e., ''nonovershooting cold pixels'') are compared with EDR observations collected within 5 min and at distances of 0–100 km from these pixels. The total number of null and turbulent EDR observations that were collected at varying distance bins (0–5, 5–10, 10–15, . . . , 75–100 km) from the two sets of pixels is determined and the frequency of light or greater, moderate or greater, and severe intensity turbulence is computed. For this study, peak EDR values of 0.10–0.19 $m^{2/3}$ s^{-1} are considered light intensity, 0.20–0.49 $m^{2/3}$ s^{-1} are considered moderate intensity, and those at and above 0.50 $m^{2/3}$ s^{-1} are considered severe intensity turbulence.

4) NLDN CLOUD-TO-GROUND LIGHTNING STRIKES

Parallax-corrected OT, nonovershooting cold pixels, and NLDN cloud-to-ground lightning strikes are compared to determine the distance between these satellite pixels and the closest CG lightning strike within a time window of ±5 min from a given satellite image. *GOES-12* IRW-texture OT detections from May to September 2008 are used in this portion of the study, as this time period represents the length of the NLDN archive collected at UW-CIMSS. When the entire satellite–NLDN comparison dataset has been processed, the radial distances of the closest lightning strikes to the satellite pixel locations are then grouped into 10-km bins between 0 and 50 km.

4. Results

a. *Qualitative comparisons between OT detections and multispectral imagery*

A representative example of output at the various processing steps of the IRW-texture OT detection algorithm is shown in Fig. 4. MODIS 1-km visible and IRW channel imagery shows multiple regions of organized convection across the upper Midwest (see Figs. 4a,b). Highly textured areas in the anvil cloud commonly associated with OTs correspond to isolated clusters of very cold (<195 K) IRW BTs. Following the procedure outlined in section 3, regions of intense convection are highlighted when the IRW BT ≤ 215 K and the GFS tropopause temperature criteria are imposed (see Fig. 4c). The spatial extent of these pixels across southern Lake Michigan and southwest Iowa is too large to exclusively represent OT pixels based upon the characteristic size of OTs noted by these authors and other prior studies. Figure 4d shows the pixels remaining after those shown in Fig. 4c are sorted by their IRW BT and spatially filtered to ensure that none are within 15 km of another. Of these pixels, those that are significantly colder than the surrounding anvil represent the final IRW-texture OT detections (see Fig. 4e). A qualitative comparison of IRW-texture OT detections with OT signatures in visible and IR channel imagery shows good agreement.

The WV-IRW BTD field shows that values between 2 and 3 K correspond well with the deep convective clouds, but also occupy too large of an area to exclusively represent OTs (see Fig. 4f). Values >3 K are generally located within the most intense convection and correlate well with pixels colder than the GFS tropopause (see Fig. 4c), but are again too widely dispersed

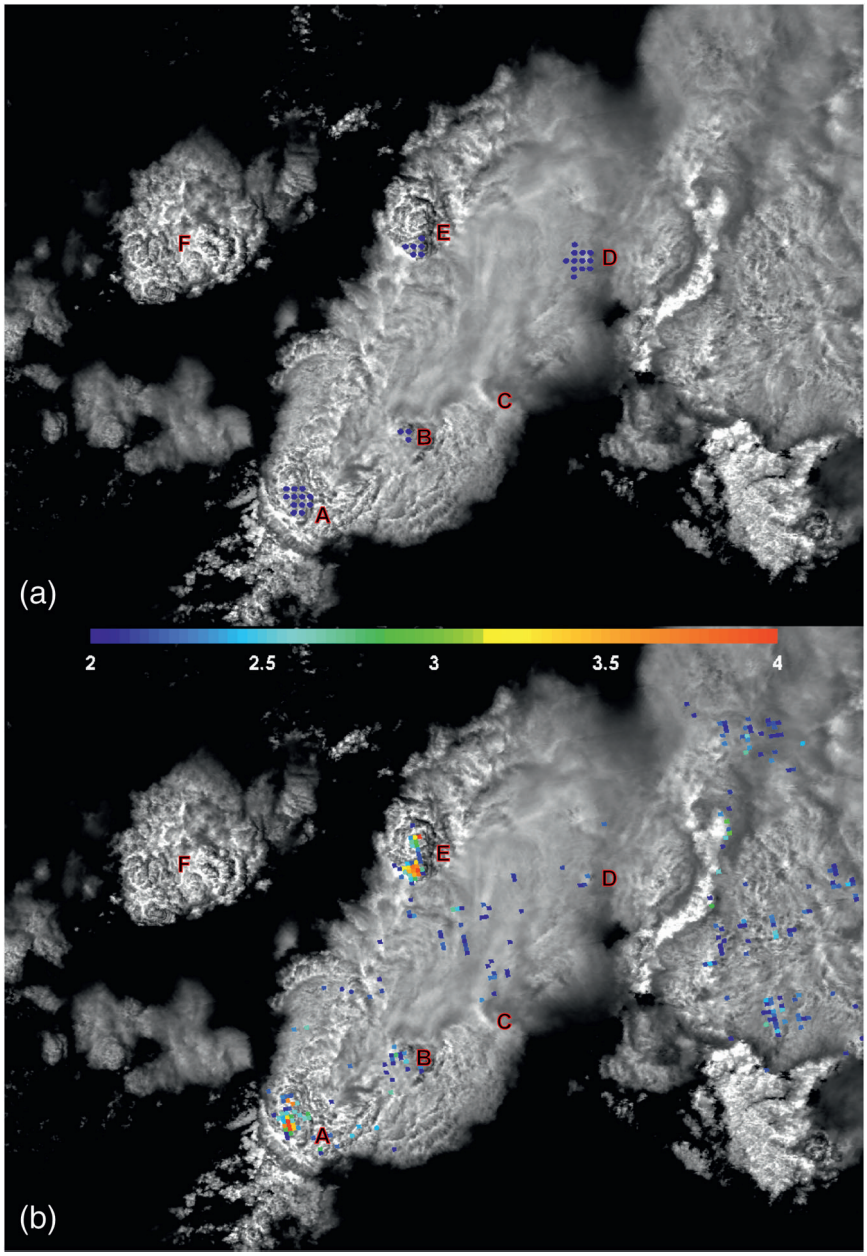

FIG. 6. (a) IRW-texture–based overshooting top detections (blue dots) for the images shown in Fig. 5. (b) The WV-IRW BTD for the same images. The color scale is provided along the top of (b). The letters A–F correspond to those of Fig. 5.

relative to the highly textured areas in the visible image (see Fig. 4a). For this case, no consistent WV-IRW BTD threshold appears to detect only what a human analyst would identify as an OT.

IRW-texture and WV-IRW BTD OT detections are also compared with *Aqua* MODIS 0.25-km visible and 1-km IRW channel imagery in Figs. 5 and 6 for a severe thunderstorm complex over western Texas to further evaluate the performance of these two methods. The 0.25-km visible image in Fig. 5a shows a highly detailed and textured set of cloud tops. The 1-km IRW image from Fig. 5b shows the presence of several clusters of cold pixels coincident with enhanced visible texture. These clusters are subjectively considered to be OTs and are labeled with letters A–E in Figs. 5a and 5b. Severe wind and hail were reported with locations A, B, and E within 20 min of the image time. An enhanced-V signature is present at location A. An above-anvil cirrus

plume, a phenomenon that has been described by Fujita (1982) and Levizzani and Setvak (1996), is present in this case and outlined in the imagery.

The IRW-texture technique identifies four of the five clusters of textured cold cloud pixels, including those associated with the enhanced-V and the remaining two severe storms (see Fig. 6a). The WV-IRW BTD approaches 4 K for locations A and E (see Fig. 6b). For the remaining human-identified OTs, the BTD varied from 2 to 3 K, which is no larger than many of the pixels scattered throughout the outlined cirrus plume or other non-OT anvil pixels. Thus, an analyst would likely infer the presence of only two OTs using the WV-IRW BTD for this case. The highly textured cloud identified by location F is not identified as overshooting by either method, and through examination of the IRW BT field, this is considered an accurate non-detection.

As the IRW-texture technique requires a significant BTD between the OT and anvil, this technique will not be able to detect as many OTs in coarser-resolution imagery because the coldest BTs for smaller OTs cannot be resolved. An example of the effect of satellite imager resolution on IRW-texture OT detection is shown in Figs. 7 and 8. Figure 7 shows a 0.25-km visible image from the same event shown in Figs. 5 and 6, but over a broader domain. Figure 8a shows that 17 individual OTs are detected when 1-km MODIS IRW imagery is used as input to the IRW-texture technique. A close inspection of these detections indicates that all are associated with an OT signature in visible imagery. Though the 4 detections shown in Fig. 6 are preserved, the number of total detections across this domain decreases from 17 to 10 when 2-km synthetic ABI is used as input (see Fig. 8b). The total number of detections decreases to three when *GOES-12* imagery is used as input (see Fig. 8c).

b. *Comparisons of MODIS OT detections with CloudSat and CALIPSO*

In this section, IRW-texture and WV-IRW BTD output are compared with collocated CloudSat and CALIPSO observations of an oceanic deep convective storm with an OT (Fig. 9a). Several distinct minima in the IRW BT field are detected by the IRW-texture method (see Fig. 9b). Figure 9c shows that the WV-IRW BTD identifies portions of several of the OTs detected by IRW-texture, but also indicates the presence of overshooting in areas away from the coldest IRW BTs.

Figure 10 shows CloudSat and CALIPSO observations and brightness temperature transects along the track shown in Fig. 9. These profiles clearly show the presence of an OT at 35°N latitude with a diameter of

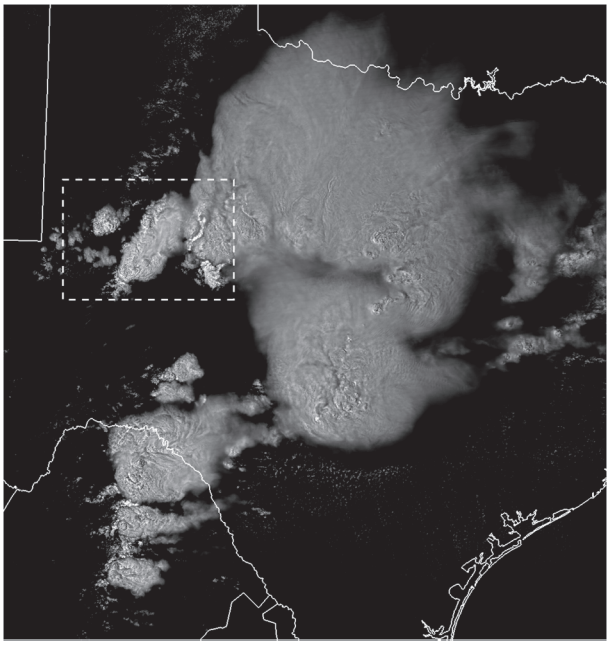

FIG. 7. *Aqua* MODIS 0.25-km visible image at 2005 UTC 13 Jun 2003 in central Texas. The domain shown in Figs. 5 and 6 is outlined with a dashed rectangle.

~8 km. The peak height of the OT is ~1.2 km above the tropopause and surrounding anvil. The IRW-texture method perfectly detected the spatial extent of the OT as depicted by CloudSat and CALIPSO. The WV-IRW BTD along the track peaked at 1.9 K in the OT, which falls just below the detection threshold described in the literature, though Fig. 9c shows that a value of ≥2 K was found very near to the track. The use of a positive BTD (i.e., >0 K) value would have identified nearly the entire anvil cloud.

The WV-IRW BTD variability in this case and shown in Figs. 4f and 6b is considerable for convection of comparable minimum IRW BT. These results show that a 2-K BTD threshold uniformly applied to all cases would result in a substantial number of false detections. This reinforces the observation that no consistent WV-IRW BTD threshold effectively identifies all OT pixels in disparate convective events. However, the IRW-texture results appear to be more consistent and spatially coherent, allowing for an unambiguous interpretation and application of product output.

c. *Quantitative comparisons between synthetic GOES-R ABI OT detections and ARW-defined truth OT pixels*

OTs identified within synthetic GOES-R ABI IRW and WV-IRW BTD imagery are compared with ARW THMR to provide a qualitative validation of these

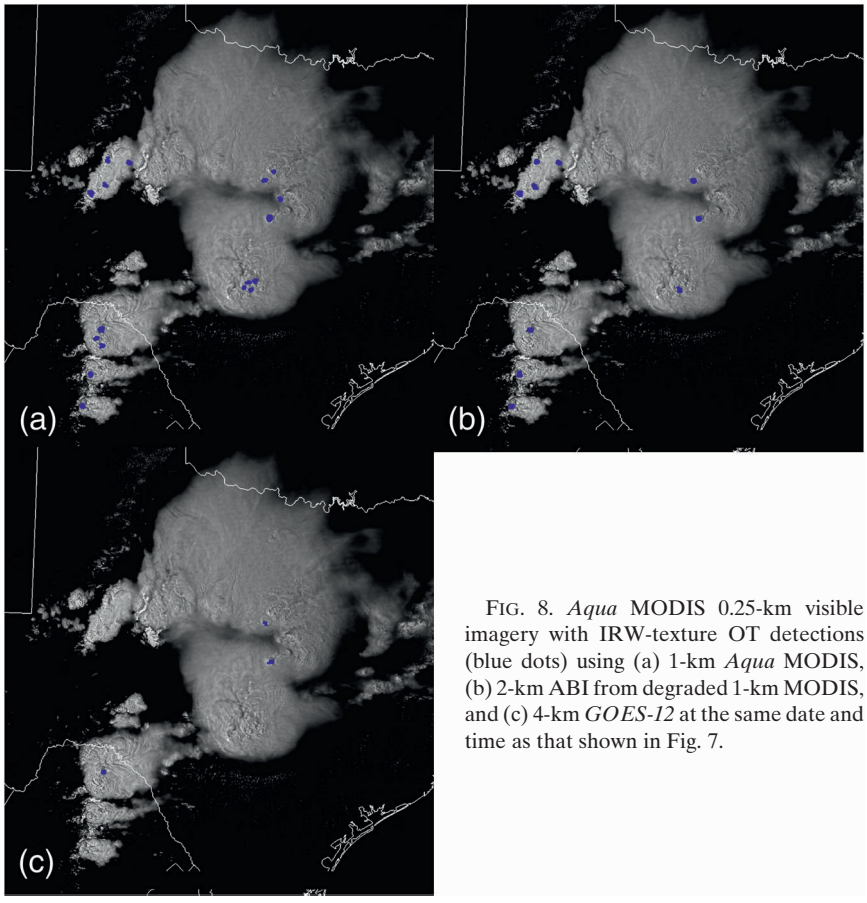

FIG. 8. *Aqua* MODIS 0.25-km visible imagery with IRW-texture OT detections (blue dots) using (a) 1-km *Aqua* MODIS, (b) 2-km ABI from degraded 1-km MODIS, and (c) 4-km *GOES-12* at the same date and time as that shown in Fig. 7.

detection techniques. An example of synthetic IRW imagery, output from the two OT detection techniques, and truth OT locations defined by ARW THMR are shown in Fig. 11 for the simulation time corresponding to 2340 UTC 4 June 2005. Figure 11a shows several regions of convection across the domain, with a minimum IRW BT of ~195 K in northeast Oklahoma, which is comparable to the cases shown in previous sections. ARW pixels with cloud tops above the tropopause (175 hPa) occupy much of the anvil cloud and those above the 165-hPa level are confined to regions with colder IRW BTs (see Fig. 11b). OT detections from the IRW-texture method show few false alarms and capture the two regions with high-confidence OTs (see Fig. 11c). Truth OTs across Illinois are completely missed by this method. OT detections from the WV-IRW BTD are fewer than those from IRW-texture, but also capture both sets of high-confidence pixels as well as portions of the storms in Illinois (see Fig. 11d).

The results of a quantitative comparison between the two OT detection techniques and truth OT locations are provided in Table 1. The results show that the BTD between the OT minimum and mean surrounding anvil BTs can be used to improve the FAR of the IRW-texture technique. Depending upon the cloud-top height considered as overshooting, the FAR improves by ~12%–19% when the required BT difference is increased from 6.5 to 10.5 K, but the total number of pixels that satisfy the more stringent criteria decreases by ~64%. Despite this substantial decrease, the percentage of high-confidence pixels detected decreases by only ~3%, which indicates that a greater OT-anvil BTD corresponds with significant vertical hydrometeor flux and higher cloud tops. When the required OT-anvil BTD is reduced, the FAR for all overshooting pixels actually improves by ~1%, but increases significantly if significant overshooting pixels are considered. Table 1 also shows that the accuracy of the IRW-texture technique is ~15%–17% better when 16 of the 16 possible surrounding anvil pixels are included in the mean. The percentage of high-confidence OT pixels is identical for both the 5 of 16 and 16 of 16 pixel criteria (not shown), suggesting that the number of valid surrounding anvil pixels can also be used as a quality control parameter.

The difference between the WV-IRW BTD FAR when the truth OT height threshold is changed from 175 to

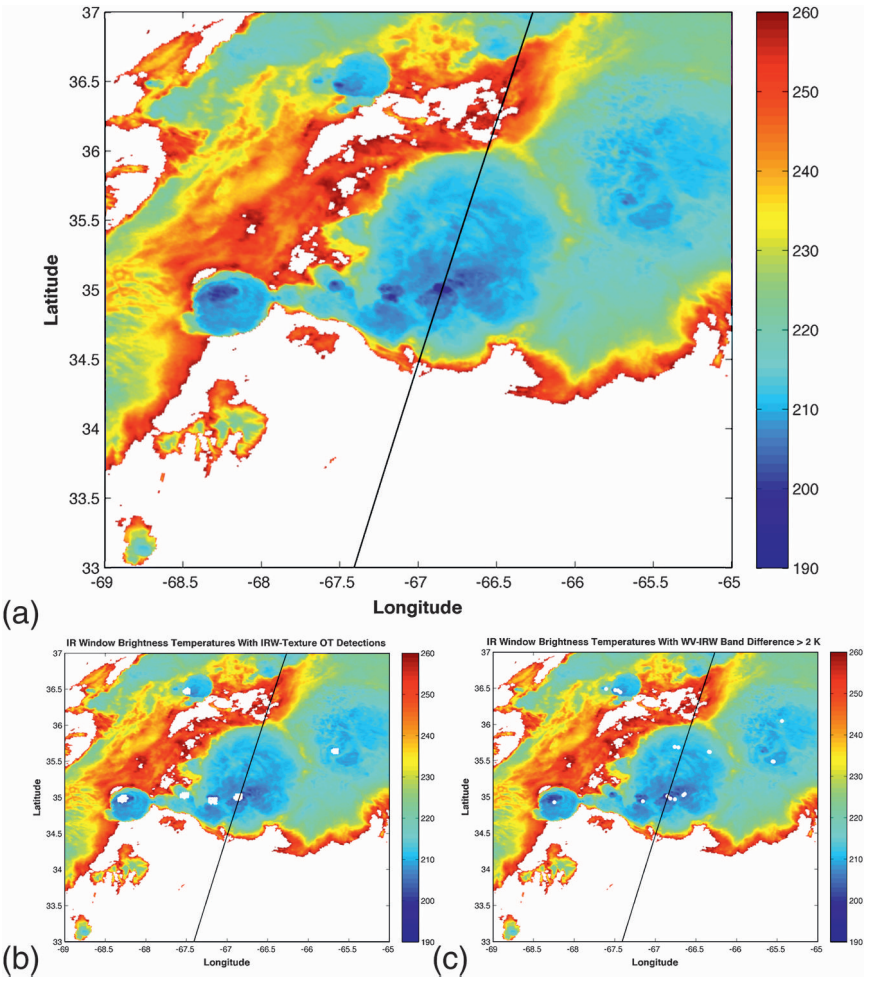

FIG. 9. (a) MODIS IRW imagery at 0630 UTC 9 Aug 2006 over the Atlantic Ocean off the North Carolina coast with the CloudSat/CALIPSO track (black line). (b) The same image with IRW-texture OT detections (white dots on color shading). (c) The same image with WV-IRW BTD $\geq$ 2 K (white dots on color shading). No OT detections were found outside the color-shaded area using either detection method.

165 hPa indicates that many of the BTD pixels correspond to an overshooting magnitude <0.5 km. This difference is not as pronounced for the IRW-texture technique. This result could be related to the findings of Schmetz et al. (1997), where they noted that the maximum WV-IRW BTD occurred with cloud tops just above the tropopause and that this BTD can decrease with greater overshooting magnitude. Though the FAR for the WV-IRW BTD is quite low for the 175-hPa truth OT threshold, the IRW-texture technique is comparable when the OT-anvil BTD is increased. For overshooting magnitudes >0.5 km, all IRW-texture algorithm settings perform better than the 2-K WV-IRW BTD. The IRW-texture outperforms the 3-K WV-IRW BTD with an 8.5-K OT-anvil BTD.

The primary difference in validation results between the two techniques is shown through the percentage of high-confidence pixels identified. For the qualitative comparisons shown in previous sections, a 3-K WV-IRW BTD is shown to be more reliable than a 2-K BTD. The detection rate for high-confidence OTs decreases significantly when this BTD threshold is adjusted from 2 to 3 K, whereas the detection rate from the IRW-texture remains fairly constant when the OT-anvil BTD is adjusted.

A maximum high-confidence OT pixel detection rate of 34.8% for IRW-texture and 28% for WV-IRW BTD suggests that some aspects of these techniques are inhibiting high-confidence pixel detection. The synthetic ABI imagery at the high-confidence OT pixel locations is analyzed here to determine why these are not being detected at a higher rate by either technique. Figure 12a shows that the reason behind the WV-IRW high-confidence pixel non-detection is straightforward in that 72% of these pixels had a WV-IRW BTD < 2 K.

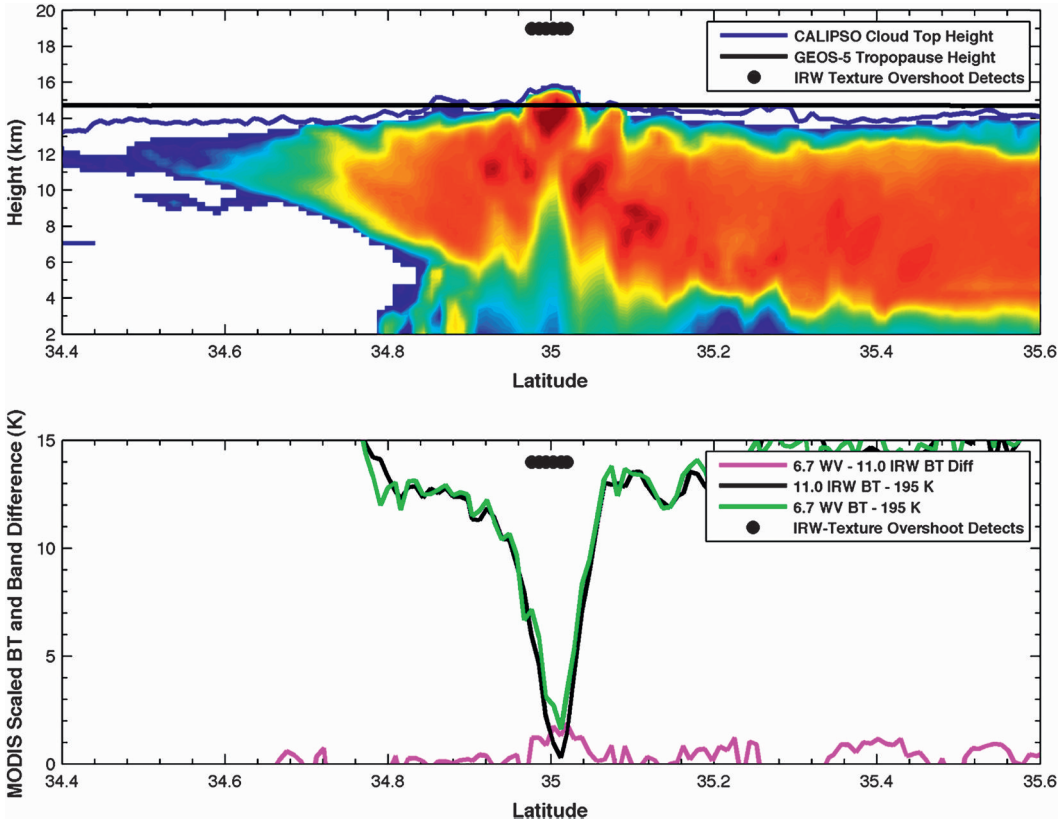

FIG. 10. (top) Collocated CloudSat Cloud Profiling Radar (color shaded), CALIPSO cloud-top height (blue line), and GEOS-5 tropopause height (black line) for the track shown in Fig. 9. IRW-texture OT detections using 2-km MODIS imagery along the CloudSat/CALIPSO track are also shown (black circles). (bottom) Scaled MODIS 1-km IRW BT (black line), WV BT (green line), and WV-IRW BT differences (magenta line) along the CloudSat/CALIPSO track with IRW-texture OT detections (black circles). IRW and WV BTs are scaled by 195, such that a BT of 195 K would appear as 0 along the *y* axis.

For the IRW-texture technique, Fig. 12b shows that all high-confidence pixels have IRW BTs $\leq$ 215 K. Figure 12c shows that the IRW BT at the high-confidence pixel location is $\leq$6.5 K colder than the mean surrounding anvil for ~26% of all observations. 9% of the high-confidence pixels were not surrounded by at least five pixels with IRW BTD $\leq$ 225 K, implying the presence of either a small or warm (i.e., >225 K) anvil cloud surrounding some high-confidence pixels (not shown). Approximately 22% of the high-confidence pixels were within 15 km of another colder candidate overshooting pixel, so these too would be excluded from detection (not shown). The remaining 12% of high-confidence pixels were left undetected because the IRW-texture method identifies pixels that are at least 50% colder than the surrounding anvil (not shown). The high-confidence OT detection percentage would increase by approximately 8%–43% if pixels 25% colder than the mean surrounding anvil BT were also considered OT pixels (not shown). This suggests that the high-confidence OTs from ARW THMR may be of larger size than those evident in the synthetic IR satellite imagery.

d. Overshooting tops in GOES-12 *imagery*

The IRW-texture technique was used to identify OTs in *GOES-12* IRW imagery from April to September 2004–08 over the eastern two-thirds of CONUS for comparison with EDR turbulence and NLDN lightning observations. The OT locations were also gridded to identify where and when OTs most often occur. The spatial distribution of OT detections during both day and night is shown in Fig. 3a. Localized maxima are present across the Southeast, the southern Great Plains, the Gulf Stream Current off the East Coast, and the higher topography of New Mexico. Minima are present over the Appalachian Mountains, New England states, and northern Rocky Mountains.

A climatology of non-overshooting cold pixels from April to September 2004–08 is provided by Fig. 13.

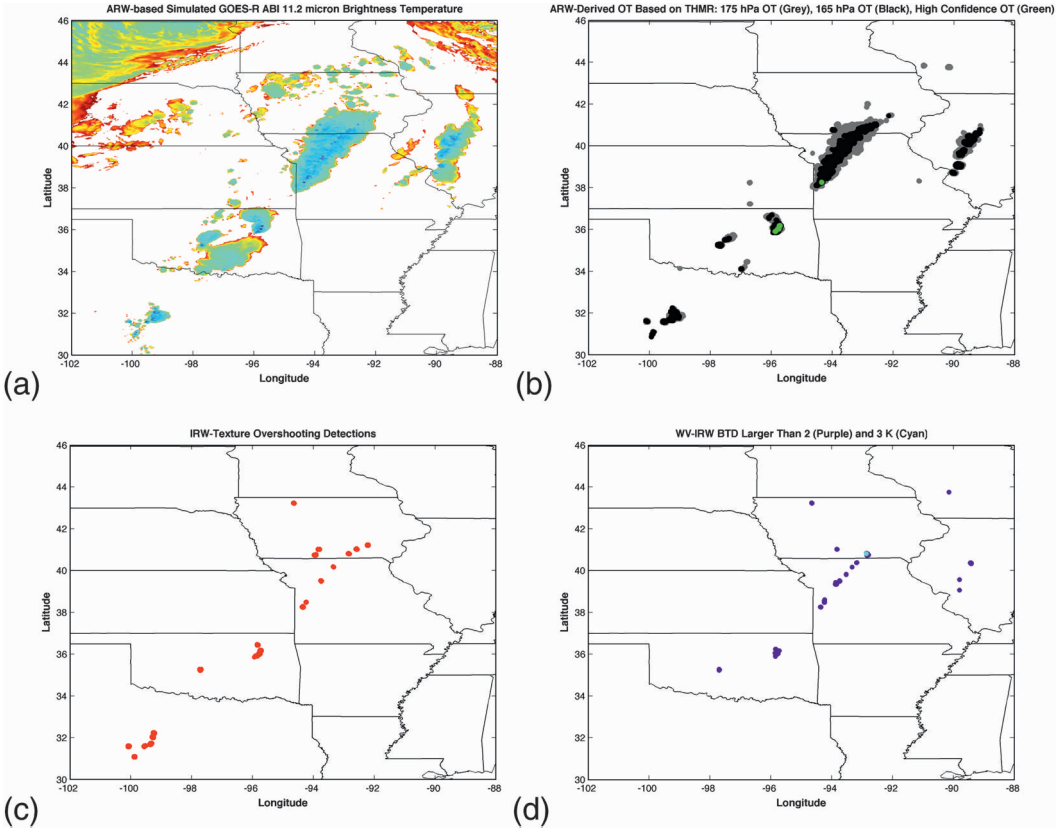

FIG. 11. (a) Synthetic GOES-R ABI 11.2-μm IRW channel imagery. The color enhancement matches that shown in Fig. 9. (b) Truth OT pixels as defined by ARW THMR. OT pixels with cloud tops above the 175-hPa level are colored in gray, pixels with tops above the 165-hPa level are colored in black, and high-confidence OT pixels are colored in green. (c) IRW-texture OT detections. (d) WV-IRW BTD values between 2 and 3 K (purple) and greater than 3 K (cyan). All images correspond to the time step at 2340 UTC 4 Jun 2005 of the ARW simulation. The cluster of high-confidence OTs in northeast Oklahoma corresponds to the clouds shown in Fig. 1.

The purpose of this is to demonstrate that the OT distribution from Fig. 3a is not simply a map of thunderstorm frequency during the above time period. The non-overshooting cold pixel climatology represents a proxy for locations of deep convective clouds with tops colder than the tropopause. If the patterns shown in Fig. 3a correlated well with those in Fig. 13, then the OT climatology could be considered a map of thunderstorm frequency and the detection algorithm may not be of significant value.

A comparison of these two climatologies indicates that this is not the case, where maxima in OT activity across Georgia and Alabama correspond to relative minima in non-overshooting cold pixels. This discrepancy is also evident across the central Great Plains where a strong maximum in non-overshooting cold pixels is collocated with OT detection counts far lower than those in many other regions across the domain. The patterns shown in Fig. 13 may be an indication of the characteristic size of BT minima of the different storm modes typically found across the United States. Storms over the Southeast during the April–September time frame are more often of the ''air mass'' variety with small IRW BT minima, whereas storms across the central Plains have an areal coverage of cold BTs far exceeding storms found in the Southeast. Since all thunderstorms do not necessarily have OTs, this OT climatology represents a unique contribution that can improve our understanding of the frequency and geographic distribution of this signature.

A comparison of OT activity differentiated by day and night is provided in Fig. 14. Figures 14a and 14b show that daytime OTs are most prominent across the eastern half of the domain and the Rocky Mountain region. Approximately 60%–80% of OTs across the Southeast occur during daytime, as frequent airmass thunderstorms develop during the afternoon hours in this region in association with strong solar heating; 60%–75% of OTs occur during the night and early morning hours over the Great Plains and western Great Lakes region

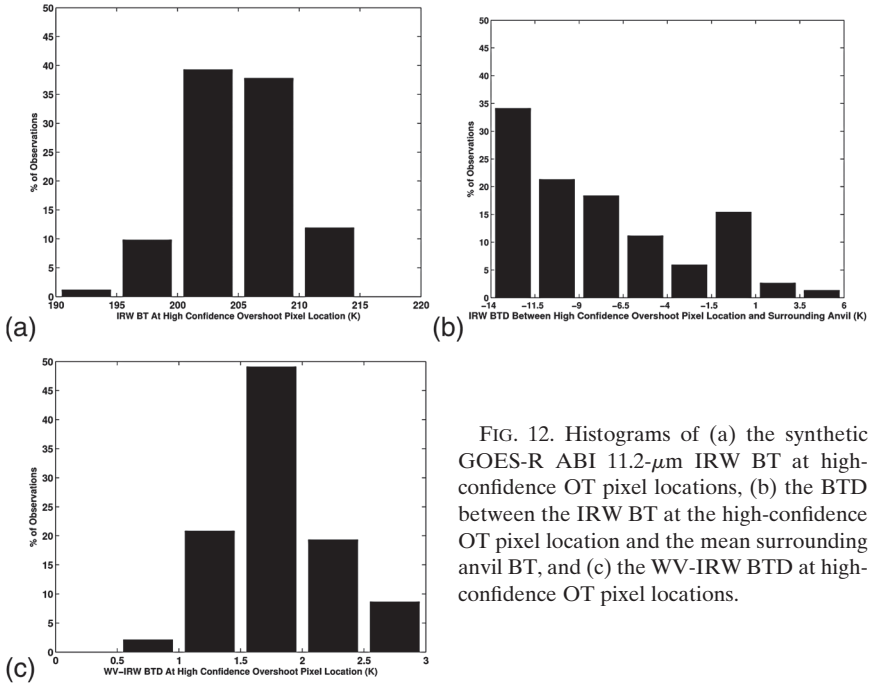

FIG. 12. Histograms of (a) the synthetic GOES-R ABI 11.2-μm IRW BT at high-confidence OT pixel locations, (b) the BTD between the IRW BT at the high-confidence OT pixel location and the mean surrounding anvil BT, and (c) the WV-IRW BTD at high-confidence OT pixel locations.

(see Figs. 14c,d). One possible explanation for this is the presence of mesoscale convective systems that often develop and propagate across this region during early evening and into the overnight hours (Maddox 1980). Interestingly, a very large number of OTs (150–200+) occurred over the Gulf Stream ocean current during both day and night, with an extension of this maximum to the northeast during the night.

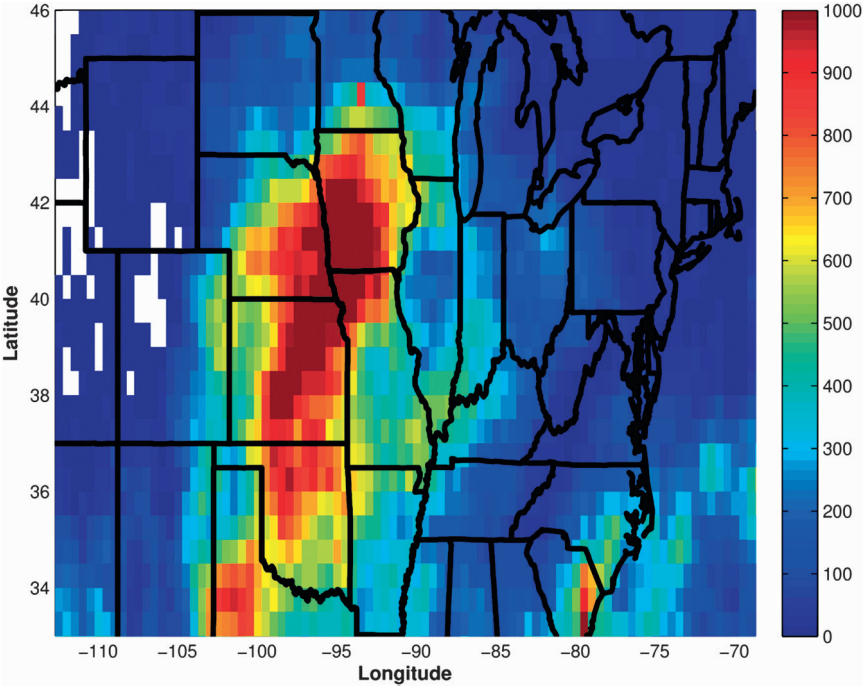

FIG. 13. A climatology of nonovershooting cold pixels from April to September 2004–08. Note the difference in color-scale limits between here and Fig. 3a.

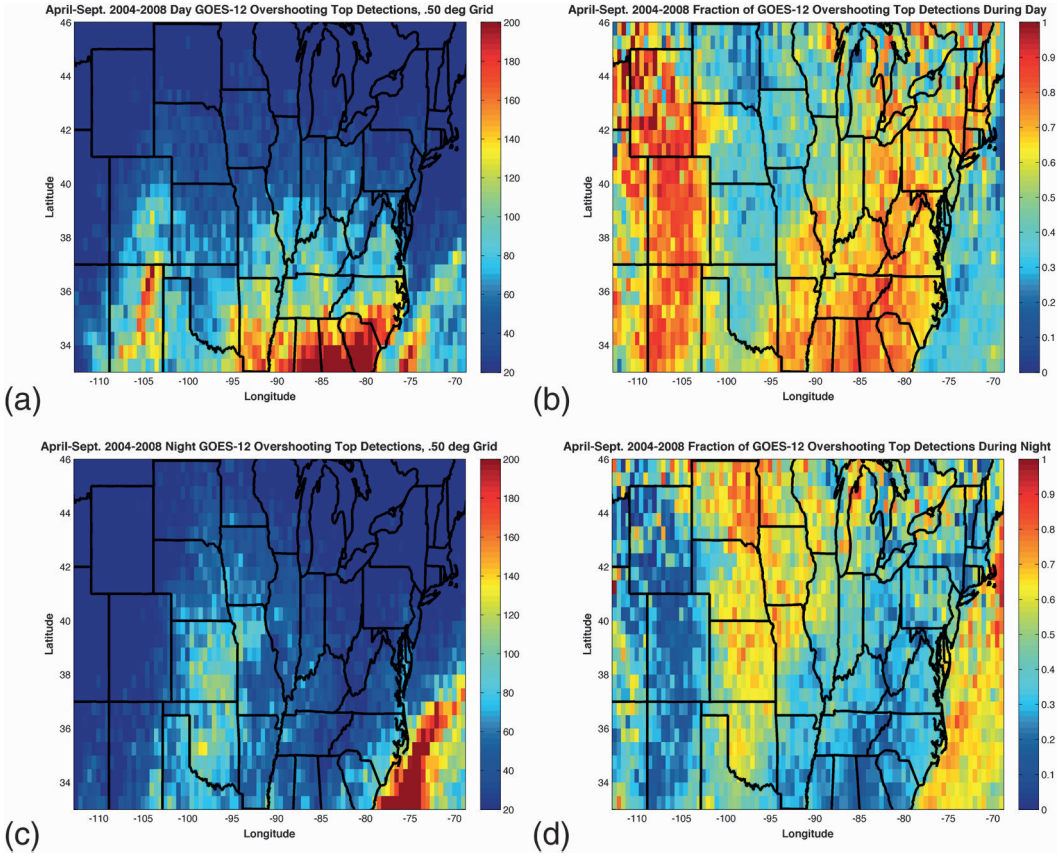

FIG. 14. (a) A climatology of OTs detected by the IRW-texture technique using *GOES-12* imagery from April to September 2004–08 for the times between 1200 and 2359 UTC. (b) The fraction of the total number of OT detections that occurred during this daytime period. (c),(d) As in (a) and (b) but for the times between 0000 and 1159 UTC.

These results show the importance of using an IR-based OT detection method because a large percentage of these events occur at night and would be missed with daytime-only algorithms. Across the Great Plains, a region with frequent United Airlines Boeing 737 and 757 flights, 20%–40% of all OT detections occurred between 9 p.m. and 12 a.m. (see Fig. 3b). The following two sections describe the relationship between OTs, lightning, and turbulence, illustrating the significant hazards posed by OT-producing storms to airline passengers and personnel.

1) COMPARISONS OF *GOES-12* OTS WITH EDR TURBULENCE

Since overshooting tops correspond with strong vertical motions and turbulent gravity waves, it would be expected that turbulence would be encountered at much greater frequency during flight near OTs. The results of the comparison between OT, nonovershooting cold pixels, and objective EDR turbulence observations are shown in Fig. 15. Light or greater intensity turbulence occurs 45% more often (42% versus 28%) when aircraft fly within 5 km of an OT relative to a nonovershooting cold pixel. Moderate or greater turbulence occurs 58% more often at this same radius and 9.5% of flights within 0–5 km of an overshoot experienced moderate or greater turbulence. Severe turbulence is quite infrequent, ~1.25% of all flights observed within a 0–5-km radius from an OT experienced severe turbulence, but this turbulence was observed 12.5 times more frequently near an OT than a nonovershooting cold pixel. These results suggest that OTs can be a significant in-flight turbulence hazard.

2) COMPARISONS OF *GOES-12* OTS WITH NLDN CLOUD-TO-GROUND LIGHTNING STRIKES

As OTs correlate well with the strongest vertical motions and charge separation in a vigorous deep convective storm, lightning activity should be found to occur more often near an OT as compared with a nonovershooting cold

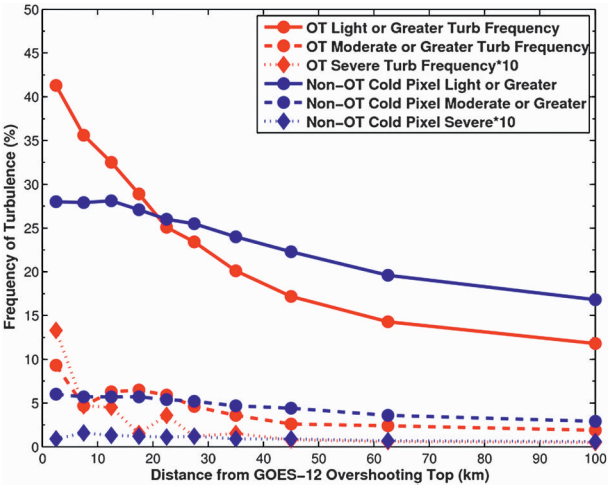

FIG. 15. The frequency of turbulence inferred through EDR observations at varying distance from *GOES-12* OT and nonovershooting cold pixels (non-OT) from April to September 2005–08 over the domain shown in Fig. 12. The frequency of severe turbulence is multiplied by 10 so that variability in the curves can be seen using the *y*-axis scale appropriate for lesser-intensity turbulence.

cloud pixel (Ziegler and MacGorman 1994; Wiens et al. 2005). A qualitative comparison of the 2004–08 OT climatology (see Fig. 3a) with the 1997–2005 annual average NLDN cloud-to-ground strike density (Wolff and Sharman 2008) illustrates many of the same patterns and supports the above hypothesis. Figure 16 provides quantitative evidence of the relationship between OT and CG lightning activity. The nearest lightning strike was within 10 km of a *GOES-12* OT for 46% of the 38 959 total top detections during May–September 2008. This compares to a 21% frequency for the 1 647 789 non-overshooting cold pixels. The nearest lightning strike was within 25 km of an overshooting (non-overshooting cold) pixel for 65% (40%) of all matches (not shown). Figure 16 also shows that the frequency of nearby lightning strikes increases significantly for very cold IRW BTs. A lightning strike occurred within a 10-km radius for 78% (55%) of overshooting (nonovershooting cold) pixels with BTs colder than 200 K. These results indicate that deep convective storms with very cold OTs identified by the IRW-texture method represent a significant cloud-to-ground lightning hazard.

5. Summary and future work

This paper describes a new technique developed at UW-CIMSS called IRW-texture that uses a combination of IRW BT minima, spatial gradients in the IRW BT field, and NWP tropopause temperature to detect OTs during both day and night in both geostationary and

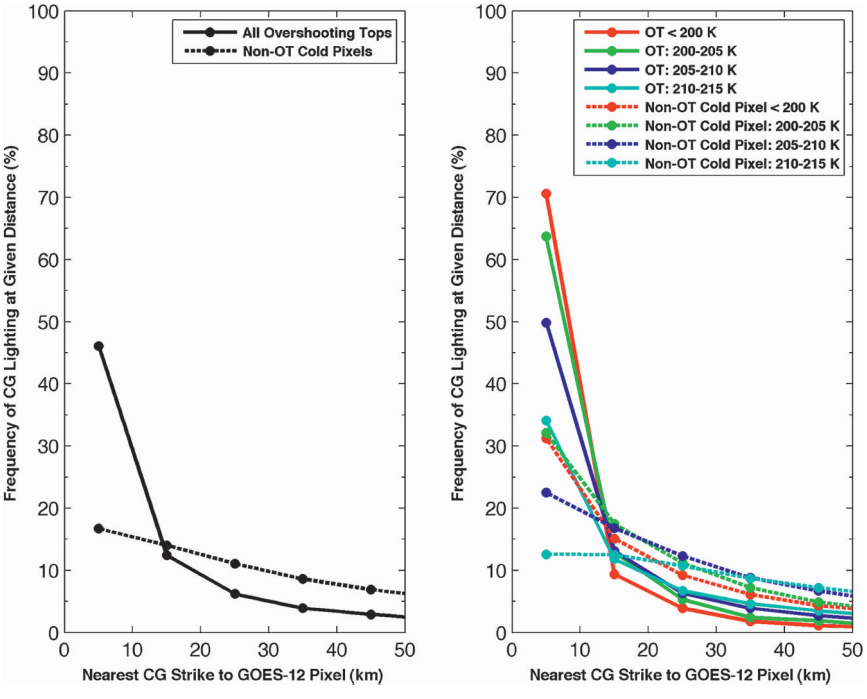

FIG. 16. (left) The distance between the closest cloud-to-ground lightning strike from May to September 2008 and both *GOES-12* IRW-texture OT detections and nonovershooting cold pixels. (right) A similar comparison to the left panel, but overshooting and nonovershooting pixels are grouped into IRW BT bins.

polar-orbiting satellite data. Comparison of OT detections with OT signatures in visible channel imagery shows that the technique performs well and that the spatial resolution of the IRW channel has a significant impact on OT detection capability. The technique is shown to perform well when applied to synthetic GOES-R ABI imagery and relative to truth OT pixels defined by ARW cloud microphysical thresholding. These comparisons show that an increased BTD between the OT and surrounding anvil and an increased number of pixels included in the surrounding anvil mean BT calculation can be used to improve the OT detection accuracy.

Validation of an alternative OT detection technique using the WV-IRW BTD indicates that 1) this technique often identifies OT regions with a spatial extent that is significantly larger than that of commonly observed OTs and 2) the required BTD threshold for OT detection is shown to be inconsistent for storms of comparable intensity. For *Aqua* MODIS, a 2-K BTD is shown to detect individual overshooting pixels in one case and a large portion of an anvil cloud in another case. An OT event observed by CloudSat and CALIPSO is detected by the IRW-texture method but was not detected through the WV-IRW BTD. Quantitative comparison between WV-IRW BTD-based detections and ARW truth OT locations shows that the BTD performs quite well for marginal OTs but this performance decreases substantially when significant OTs are considered. Based upon the qualitative and quantitative comparisons shown in this study, we conclude that the IRW-texture technique offers a more consistent day/night OT detection capability than other existing methods, allowing for unambiguous interpretation and application of product output for aviation and severe weather forecasting.

A 5-yr *GOES-12* IRW-texture OT climatology shows OT maxima across the Southeast, southern Great Plains, Gulf Stream ocean current, and higher topography of New Mexico, which is consistent with locations of frequent deep convective storms across the eastern two-thirds of the United States. The frequency and regional distribution of OTs are shown to vary between day and night, which may be related to diurnal differences in convective regimes across the United States (i.e., daytime orographically induced or air mass thunderstorms versus nighttime mesoscale convective systems). These results show the importance of using an IR-based OT detection method because 60%–75% of these events occur at night over the Great Plains and western Great Lakes region and would be missed by daytime-only algorithms.

GOES-12 OTs identified by the IRW-texture method are shown in this study to represent a significant cloud-to-ground lightning hazard and are good indicators of the potential for nearby in-flight turbulence. When IRW-texture OT pixels are directly compared with nearby NLDN observations, CG lightning is found to occur within a 10-km radius of an OT 1.2 times more often than a non-overshooting cold cloud pixel. For very cold OTs with IRW BTs less than 200 K, CG lightning occurred nearby for 70% of all OT occurrences. The results show that aircraft that flew within 5 km of an OT experienced turbulence in 42% of all encounters—a 45% increase in turbulence frequency relative to flights near non-overshooting cloud pixels. Moderate–severe turbulence was also experienced at a higher frequency in these close OT encounters.

Future work involves using OTs identified by the IRW-texture technique as the foundation of an objective enhanced-V signature detection algorithm for the GOES-R ABI program. Validation of OT detections using a combination of NASA TRMM 2-km-resolution Visible Infrared Scanner (VIRS) and precipitation radar instrument data would provide additional insight into the accuracy of this detection technique at a spatial resolution that matches that of GOES-R ABI. OT climatologies may also be produced for other satellite imagers such as the MSG SEVIRI and/or Multifunction Transport Satellite (MTSAT) to better understand the temporal and spatial distribution of OT occurrences worldwide. As three-dimensional total lightning networks such as the Northern Alabama Lightning Mapping Array (LMA; Koshak et al. 2004) and satellite-based lightning observations from the GOES-R Geostationary Lightning Mapper (GLM) become increasingly available, we can expand this research toward better understanding the relationship between satellite-observed OTs and total lightning activity. Cloud-resolving NWP modeling and synthetic satellite imagery can be combined to better understand and objectively estimate the amount of water vapor injected into the stratosphere by OTs. If satellite imagery can provide an objective indication of the magnitude of this transport, the results from the aforementioned global OT climatology can be combined with this information to better understand the effects of deep convection on the climate system.

Acknowledgments. This research was supported by NASA decision support CAN Award AGR DTD 5/18/06. The authors thank Robert Sharman, John Williams, and NCAR RAL support staff for the EDR datasets and exchange of ideas on convectively induced turbulence processes. The ARW model simulation was performed on the ''cobalt'' supercomputer at the National Center for Supercomputing Applications at the University of Illinois at Urbana–Champaign. The authors thank the UW-SSEC McIDAS-V development team for their

visualization support, Liam Gumley for providing some of the MODIS data used in this paper, and the SSEC Data Center for the large volumes of *GOES-12* data used in the overshooting top climatology. The authors also thank Scott Lindstrom (UW-SSEC) for providing software to properly simulate future GOES-R ABI imagery from existing MODIS imagery.

REFERENCES

Ackerman, S. A., 1996: Global satellite observations of negative brightness temperature differences between 11 and 6.7 μm. *J. Atmos. Sci.,* **53,** 2803–2812.

Adler, R. F., and R. A. Mack, 1986: Thunderstorm cloud top dynamics as inferred from satellite observations and a cloud top parcel model. *J. Atmos. Sci.,* **43,** 1945–1960.

——, M. J. Markus, D. D. Fen, G. Szejwach, and W. E. Shenk, 1983: Thunderstorm top structure observed by aircraft overflights with an infrared radiometer. *J. Climate Appl. Meteor.,* **22,** 579–593.

——, ——, and D. D. Fenn, 1985: Detection of severe Midwest thunderstorms using geosynchronous satellite data. *Mon. Wea. Rev.,* **113,** 769–781.

Bedka, K. M., W. F. Feltz, J. R. Mecikalksi, R. D. Sharman, A. Lenz, and J. Gerth, 2007: Satellite signatures associated with significant convectively-induced turbulence events. *Proc. Joint Meteorological Satellite and 15th Satellite Meteorology and Oceanography Conf.,* Amsterdam, Netherlands, EUMETSAT and Amer. Meteor. Soc. [Available online at http://www.eumetsat.int/Home/Main/AboutEUMETSAT/Publications/ConferenceandWorkshopProceedings/2007/SP_1232700283028?l=en.]

Berendes, T. A., J. R. Mecikalski, W. M. MacKenzie Jr., K. M. Bedka, and U. S. Nair, 2008: Convective cloud identification and classification in daytime satellite imagery using standard deviation limited adaptive clustering. *J. Geophys. Res.,* **113,** D20207, doi:10.1029/2008JD010287.

Brunner, J. C., S. A. Ackerman, A. S. Bachmeier, and R. M. Rabin, 2007: A quantitative analysis of the enhanced-V feature in relation to severe weather. *Wea. Forecasting,* **22,** 853–872.

Chemel, C., M. R. Russo, J. A. Pyle, R. S. Sokhi, and C. Schiller, 2008: Quantifying the imprint of a severe hector thunderstorm during ACTIVE/SCOUT-O3 onto the water content in the upper troposphere/lower stratosphere. *Mon. Wea. Rev.,* **137,** 2493–2514.

Cornman, L. B., and B. Carmichael, 1993: Varied research efforts are under way to find means of avoiding air turbulence. *ICAO J.,* **48,** 10–15.

——, C. S. Morse, and G. Cunning, 1995: Real-time estimation of atmospheric turbulence severity from in-situ aircraft measurements. *J. Aircr.,* **32,** 171–177.

FAA, cited 2004: Review of aviation accidents involving weather turbulence in the United States, 1992-2001. National Aviation Safety Data Analysis Center Doc. 04-551, FAA Office of System Safety. [Available online at http://www.asias.faa.gov/aviation_studies/turbulence_study/turbulence_study_new.pdf.]

Fritz, S., and I. Laszlo, 1993: Detection of water vapor in the stratosphere over very high clouds in the tropics. *J. Geophys. Res.,* **98** (D12), 22 959–22 967.

Fujita, T. T., 1982: Principle of stereoscopic height computations and their applications to stratospheric cirrus over severe thunderstorms. *J. Meteor. Soc. Japan,* **60,** 355–368.

——, 1992: Memoirs of an effort to unlock the mystery of severe storms. WRL Research Paper 239, University of Chicago Wind Research Lab, 298 pp.

Glickman, T., Ed., 2000: *Glossary of Meteorology*. 2nd ed. Amer. Meteor. Soc., 855 pp.

Heidinger, A. K., C. O'Dell, R. Bennartz, and T. Greenwald, 2006: The successive-order-of-interaction radiative transfer model. Part I: Model development. *J. Appl. Meteor. Climatol.,* **45,** 1388–1402.

Heymsfield, G. M., R. Fulton, and J. D. Spinhirne, 1991: Aircraft overflight measurements of Midwest severe storms: Implications and geosynchronous satellite interpretations. *Mon. Wea. Rev.,* **119,** 436–456.

Hoinka, K. P., 1999: Temperature, humidity, and wind at the global tropopause. *Mon. Wea. Rev.,* **127,** 2248–2265.

Koshak, W. J., and Coauthors, 2004: North Alabama Lightning Mapping Array (LMA): VHF source retrieval algorithm and error analyses. *J. Atmos. Oceanic Technol.,* **21,** 543–558.

Kummerow, C., and W. Barnes, 1998: The tropical rainfall measuring mission (TRMM) sensor package. *J. Atmos. Oceanic Technol.,* **15,** 809–817.

Lane, T. P., R. D. Sharman, T. L. Clark, and H. M. Hsu, 2003: An investigation of turbulence generation mechanisms above deep convection. *J. Atmos. Sci.,* **60,** 1297–1321.

Lazzara, M. A., and Coauthors, 1999: The Man computer Interactive Data Access System: 25 years of interactive processing. *Bull. Amer. Meteor. Soc.,* **80,** 271–284.

Levizzani, V., and M. Setvak, 1996: Multispectral, high-resolution satellite observations of plumes on top of convective storms. *J. Atmos. Sci.,* **53,** 361–369.

Lindsey, D. T., and L. Grasso, 2008: An effective radius retrieval for thick ice clouds using GOES. *J. Appl. Meteor. Climatol.,* **47,** 1222–1231.

Lindstrom, S. S., C. C. Schmidt, E. M. Prins, J. Hoffman, J. Brunner, and T. J. Schmit, 2008: Proxy ABI datasets relevant for fire detection that are derived from MODIS data. Preprints, *Fifth GOES Users's Conf.,* New Orleans, LA, Amer. Meteor. Soc., P1.35. [Available online at http://ams.confex.com/ams/pdfpapers/132606.pdf.]

Liu, C., and E. J. Zipser, 2005: Global distribution of convection penetrating the tropical tropopause. *J. Geophys. Res.,* **110,** D23104, doi:10.1029/2005JD006063.

Maddox, R. A., 1980: Mesoscale convective complexes. *Bull. Amer. Meteor. Soc.,* **61,** 1374–1387.

Martin, D. W., R. A. Kohrs, F. R. Mosher, C. M. Medaglia, and C. Adamo, 2008: Over-ocean validation of the Global Convective Diagnostic. *J. Appl. Meteor. Climatol.,* **47,** 525–543.

Mitrescu, C., S. Miller, J. Hawkins, T. L'Ecuyer, J. Turk, P. Partain, and G. Stephens, 2008: Near-real-time applications of CloudSat data. *J. Appl. Meteor. Climatol.,* **47,** 1982–1994.

Negri, A. J., 1982: Cloud-top structure of tornado storms on 10 April 1979 from rapid scan and stereo satellite observations. *Bull. Amer. Meteor. Soc.,* **63,** 1851–1859.

——, and R. F. Adler, 1981: Relation of satellite-based thunderstorm intensity to radar-estimated rainfall. *J. Appl. Meteor.,* **20,** 288–300.

Orville, R. E., 2008: Development of the National Lightning Detection Network. *Bull. Amer. Meteor. Soc.,* **89,** 180–190.

Otkin, J. A., T. J. Greenwald, J. Sieglaff, and H. L. Huang, 2009: Validation of a large-scale simulated brightness temperature dataset using SEVIRI satellite observations. *J. Appl. Meteor. Climatol.,* **48,** 1613–1626.

Reynolds, D. W., 1980: Observations of damaging hailstorms from geosynchronous satellite digital data. *Mon. Wea. Rev.,* **108,** 337–348.

Rosenfeld, D., W. L. Woodley, A. Lerner, G. Kelman, and D. T. Lindsey, 2008: Satellite detection of severe convective storms by their retrieved vertical profiles of cloud particle effective radius and thermodynamic phase. *J. Geophys. Res.,* **113,** D04208, doi:10.1029/2007JD008600.

Schmetz, J., S. A. Tjemkes, M. Gube, and L. van de Berg, 1997: Monitoring deep convection and convective overshooting with METEOSAT. *Adv. Space Res.,* **19,** 433–441.

——, P. Pili, S. Tjemkes, D. Just, J. Kerkmann, S. Rota, and A. Ratier, 2002: An introduction to Meteosat Second Generation (MSG). *Bull. Amer. Meteor. Soc.,* **83,** 977–992.

Schmit, T. J., M. M. Gunshor, W. P. Menzel, J. J. Gurka, J. Li, and A. S. Bachmeier, 2005: Introducing the next-generation Advanced Baseline Imager on GOES-R. *Bull. Amer. Meteor. Soc.,* **86,** 1079–1096.

Setvak, M., R. M. Rabin, and P. K. Wang, 2007: Contribution of the MODIS instrument to observations of deep convective storms and stratospheric moisture detection in GOES and MSG imagery. *Atmos. Res.,* **83,** 505–518.

——, D. T. Lindsey, P. Novak, R. M. Rabin, P. K. Wang, J. Kerkmann, M. Radova, and J. Stastka, 2008a: Cold-ring shaped storms in central Europe. *Proc. 2008 EUMETSAT Meteorological Satellite Conf.,* Darmstadt, Germany, EUMETSAT. [Available online at http://www.eumetsat.int/Home/Main/AboutEUMETSAT/Publications/ConferenceandWorkshopProceedings/2008/SP_1232700911980?l=en.]

——, ——, R. M. Rabin, P. K. Wang, and A. Demeterova, 2008b: Indication of water vapor transport into the lower stratosphere above midlatitude convective storms: Meteosat Second Generation satellite observations and radiative transfer model simulations. *Atmos. Res.,* **89,** 170–180.

Sharman, R., L. Cornman, J. K. Williams, S. E. Koch, and W. R. Moninger, 2006: The FAA AWRP Turbulence PDT. Preprints, *12th Conf. on Aviation Range and Aerospace Meteorology,* Atlanta, GA, Amer. Meteor. Soc., 3.3. [Available online at http://ams.confex.com/ams/pdfpapers/104014.pdf.]

Skamarock, W. C., J. B. Klemp, J. Dudhia, D. O. Gill, D. M. Barker, W. Wang, and J. G. Powers, 2007: A description of the Advanced Research WRF Version 2. NCAR Tech. Note NCAR/TN-468+STR, 100 pp.

Stephens, G. L., and CloudSat Science Team, 2002: The CloudSat mission and the A-Train. *Bull. Amer. Meteor. Soc.,* **83,** 1771–1790.

Wang, P. K., 2003: Moisture plumes above thunderstorm anvils and their contributions to cross-tropopause transport of water vapor in midlatitudes. *J. Geophys. Res.,* **108,** 4194, doi:10.1029/2002JD002581.

Wiens, K. C., S. A. Rutledge, and S. A. Tessendorf, 2005: The 29 June 2000 supercell observed during STEPS. Part II: Lightning and charge structure. *J. Atmos. Sci.,* **62,** 4151–4177.

Wolff, J. K., and R. D. Sharman, 2008: Climatology of upper-level turbulence over the contiguous United States. *J. Appl. Meteor. Climatol.,* **47,** 2198–2214.

Ziegler, C. L., and D. R. MacGorman, 1994: Observed lightning morphology relative to modeled space charge and electric field distributions in a tornadic storm. *J. Atmos. Sci.,* **51,** 833–851.